Conduction and convection analyses of flexible electronic devices via coupled thermo-elastic formulation and variable-fidelity beam models

Journal of Thermal Stresses

ISSN: 0149-5739 (Print) 1521-074X (Online) Journal homepage: www.tandfonline.com/journals/uths20

Conduction and convection analyses of flexible electronic devices via coupled thermo-elastic formulation and variable-fidelity beam models

R. Azzara, M. Filippi, A. Racionero Sánchez-Majano & E. Carrera

To cite this article: R. Azzara, M. Filippi, A. Racionero Sánchez-Majano & E. Carrera (01 Jun 2026): Conduction and convection analyses of flexible electronic devices via coupled thermo-elastic formulation and variable-fidelity beam models, Journal of Thermal Stresses, DOI: 10.1080/01495739.2026.2630210

To link to this article: https://doi.org/10.1080/01495739.2026.2630210

Published online: 01 Jun 2026.

JOURNAL OF THERMAL STRESSES
https://doi.org/10.1080/01495739.2026.2630210

Taylor & Francis
Taylor & Francis Group

Conduction and convection analyses of flexible electronic devices via coupled thermo-elastic formulation and variable-fidelity beam models

R. Azzara[a], M. Filippi[a], A. Racionero Sánchez-Majano[b], and E. Carrera[a]

[a]MUL^2*Lab*, Department of Mechanical and Aerospace Engineering, Politecnico di Torino, Torino, Italy; [b]Department of Aerospace Engineering, Universidad Carlos III de Madrid, Leganés-Madrid, Spain

ABSTRACT

This work presents one-dimensional (1D) beam kinematic models with variable fidelity for analyzing coupled thermo-elastic problems in components of electronic interest. By employing the Carrera Unified Formulation (CUF), the proposed methodology enables accurate predictions of displacements, stresses, and temperature distributions in homogeneous isotropic structures subjected to complex heat sources. Transforming the complex three-dimensional (3D) problem into a computationally efficient one-dimensional (1D) framework allows for an optimal balance between accuracy and low computational cost. Classical thermo-elasticity theories are adopted to describe the physical behavior, and the formulation is applied to various flexible electronic components to demonstrate its versatility. Several numerical simulations, including convergence studies and validation against full 3D solid models, confirm the reliability and accuracy of the proposed technique. The results highlight the method's strong potential for guiding and accelerating the design and fabrication of next-generation flexible electronic devices (FEDs) in advanced engineering applications.

ARTICLE HISTORY
Received 27 January 2026
Accepted 4 February 2026

KEYWORDS
Carrera unified Formulation; coupled thermo-elasticity; finite element method; flexible electronic devices; refined beam models

1. Introduction

Nowadays, numerous engineering applications rely on the presence of integrated electronic devices needing higher integration densities and power demands. As these electronics operate, they act as heat sources, generating thermal gradients and subsequent thermal stresses due to the differences in the coefficient of thermal expansion (CTE) among the materials used to fabricate these devices. In this regard, the interplay between thermal and mechanical effects necessitates a thermo-mechanical analysis capable of providing an accurate prediction of thermal and stress gradients to ensure the reliability, performance, and lifespan of electronic systems.

Pioneering studies on the thermo-mechanical analysis of electronic systems were performed by Feng and Wu [1]. These authors conducted a decoupled analysis where the thermal steady state was input into the elasticity problem. They proposed closed-form solutions to calculate the interfacial thermal stresses and edge effect, and conducted a parametric study involving various geometrical dimensions of the chip and the substrate. Likewise, Wu [2] emphasized the importance of accurately calculating free-edge thermal stresses, which can be detrimental as they may lead to

CONTACT R. Azzara rodolfo.azzara@polito.it MUL^2*Lab*, Department of Mechanical and Aerospace Engineering, Politecnico di Torino, Corso Duca degli Abruzzi 24, 10129 Torino, Italy.

cracking or delamination, ultimately resulting in failure or malfunction of the electronic assembly. Quirino *et al.* [3] conducted detailed thermal analyses of the HERMES cubesat payload, with particular attention to evaluating the performance of newly developed passive thermal links. Jeyaraj *et al.* [4] presented transient thermo-structural analysis of un-submerged flex nozzle system. Lim *et al.* [5] investigated the deformation and warping behavior of thin-layered semiconductor structures incorporating a silicon substrate.

Similarly, in recent years, flexible electronic devices (FEDs) have attracted the attention of researchers as they enhance the potential for practical use in epidermal and bio-optoelectronics, which are able to real-time, efficiently and conveniently monitor vital signs of the human body like electrocardiograph and electroencephalogram [6], blood flow [7], temperature [8,9], oxygen [10], and glucose [8,11], among others. FEDs are composed of various constituents, including the polymeric substrate, conductive traces, encapsulants, and semiconductor elements. These elements present mismatching thermal conductivities and CTEs, which lead to large thermal gradients and their corresponding thermal strains, and ultimately may induce delaminations, cracking, or plastic deformations. To limit the occurrence of these failure mechanisms, accurate thermo-mechanical analyses are needed to identify the heat transfer mechanisms and minimize the adverse effects. For instance, Lu *et al.* [12] derived an analytical axisymmetric model to study the thermal behavior of μ-ILED, establishing a scaling law for the design of μ-ILED devices. Sakai *et al.* [13] conducted a series of Finite Element Analyses (FEA) to find the breaking point at the boundary between the organic layer and the contact electrode. Kang *et al.* [14] validated an FE model with experimental results for sensors inspired by a spider's sensory system, presenting applications such as the detection of physiological signals or highly selective speech pattern recognition. Cui *et al.* [15] studied the discomfort avoidance in epidermal electronic devices (EEDs) by developing a three-dimensional analytical model of their integration with human skin, aiming to optimize device layout for improved user comfort. A review of the synergistic frontier for flexible electronics was provided by Zhong *et al.* [16]. Other recent and relevant studies on flexible devices can be found in Refs. [17–19].

The aforementioned works, albeit pivotal in the study of electronic devices, relied on the derivation of closed-form solutions, hence limiting the range of applications, or on the use of expensive three-dimensional (3D) FE models. Additionally, many of them considered decoupled thermal and mechanical fields, hindering the precision of the proposed approaches. To circumvent these limitations, the current manuscript proposes a fully coupled thermo-mechanical analysis solved through an efficient one-dimensional (1D) FE method with tunable accuracy. The latter characteristic is achieved by exploiting the Carrera Unified Formulation (CUF) [20]. CUF allows the generation of scalable low- to high-fidelity structural theories in a straightforward and systematic manner, without the need to rewrite the governing equations of the problem. Additionally, when CUF is combined with FEM, it allows for preserving the original FE discretization and selecting the solution accuracy as input to the analysis. In recent years, the governing equations of coupled thermo-elasticity have been written in CUF form, see [21,22]. In detail, CUF has been used to tackle problems in Functionally Graded Materials [23], multi-layered plates and shells [24], and transient thermo-elastic analyses of truss-like structures [25]. This document proposes a numerical framework that combines CUF with 1D FE models to investigate the coupled static thermo-elasticity problem in electronic devices. In contrast to the above-mentioned works, which focused on thermo-elasticity in plates, shells, truss-like structures, or generic multilayer components, the novelty of the present study lies in: 1) a dedicated CUF-based framework for FEDs, including both external and integrated chip configurations, which have not been previously addressed in the CUF thermo-elastic literature; 2) a fully coupled conduction-convection-radiation formulation integrated into 1D CUF models, enabling the prediction of temperature fields and thermal stresses in devices where heat transfer is strongly dominated by surface effects; 3) a quantitative assessment of accuracy versus computational cost, showing significant reductions in degrees of freedom compared to 3D solid models, while maintaining the accuracy of temperature gradients, displacements, stress distributions, and strain fields; 4) a systematic study of kinematic fields in thermo-elastic problems, demonstrating how different lower- and higher-order models influence the prediction of thermal gradients and deformation in multilayer electronic components.

The manuscript is structured as follows: Section 2 provides the governing equations of the coupled thermo-mechanical problem, its FE formulation and the combination with CUF to generate arbitrary structural models; Section 3 shows the application of the proposed framework to various electronic components subject to mechanical and thermal loading conditions, and Section 4 summarizes the key findings.

2. Coupled thermo-elasticity problem

2.1. Governing equations

The equation of motion of a 3D elastic body in a Cartesian reference frame reads as:

$$\nabla \cdot \boldsymbol{\sigma} + \mathbf{b} = \rho \ddot{\mathbf{u}}, \tag{1}$$

where $\boldsymbol{\sigma}$ and $\mathbf{u}$ denote the stress tensor and the field of displacements vector, $\mathbf{b}$ are the body forces per unit volume, and ρ is the mass density [26]. Additionally, the strain-displacement relations within the linear context of small deformation theory read as:

$$\boldsymbol{\varepsilon} = \frac{1}{2}(\nabla \mathbf{u} + \nabla \mathbf{u}^{\mathrm{T}}). \tag{2}$$

Then, Hooke's law for a non-homogeneous anisotropic thermo-elastic material can be written as:

$$\boldsymbol{\sigma} = \mathbf{C}\boldsymbol{\varepsilon} - \boldsymbol{\beta}\mathrm{T}, \tag{3}$$

in which $\mathbf{C}$ is the fourth-order elasticity tensor of a non-homogeneous anisotropic material, $\boldsymbol{\beta} = \mathbf{C}\boldsymbol{\alpha}$ is the second-order tensor of thermo-elastic moduli, being $\boldsymbol{\alpha}$ the second-order thermal expansion tensor, and T is the temperature change relative to the stress-free reference temperature T_0.

The energy balance equation is expressed as:

$$\nabla \cdot \mathbf{q} = Q - \mathrm{T}_0 \dot{S}, \tag{4}$$

where $\mathbf{q}$ is the heat flux vector, Q is the internal heat source per unit volume. S is the entropy per unit volume and is given by:

$$S = \frac{\rho c_p}{\mathrm{T}_0}\mathrm{T} + \boldsymbol{\beta}^{\mathrm{T}}\boldsymbol{\varepsilon}, \tag{5}$$

where c_p is the specific heat at constant pressure. Furthermore, recalling that the heat conduction equation for an anisotropic material can be stated as:

$$\mathbf{q} = -\boldsymbol{\kappa}\nabla\mathrm{T}, \tag{6}$$

where $\boldsymbol{\kappa}$ is the second-order thermal conductivity tensor.

Incorporating Equation (3) into Equation (1), and Equations (5) and (6) in Equation (4), the thermo-elasticity coupled problem reads as:

$$\nabla \cdot \boldsymbol{\sigma} + \mathbf{b} = \rho \ddot{\mathbf{u}}, \tag{7}$$

$$\rho c_p \frac{\partial \mathrm{T}}{\partial t} - \nabla \cdot (\boldsymbol{\kappa}\nabla\mathrm{T}) + \mathrm{T}_0 \boldsymbol{\beta}^{\mathrm{T}}\dot{\boldsymbol{\varepsilon}} = Q. \tag{8}$$

This system of equations comprises three equations of motion and one heat conduction equation, under specified initial and boundary conditions, which must be simultaneously solved to retrieve the three unknown displacement components and the temperature change of the solid. In Equations (7) and (8), the coupling between the mechanical and thermal fields is explicitly introduced through the thermoelastic moduli $\boldsymbol{\beta}$. In the constitutive equation, the term $-\boldsymbol{\beta}\mathrm{T}$ represents the thermal contribution to the stress field, i.e., the stresses induced by temperature variations in the presence of thermal expansion. This term describes the thermo-mechanical coupling, in which non-uniform temperature fields generate additional strains and stresses. In contrast, in the energy balance equation, the term $\mathrm{T}_0\boldsymbol{\beta}^{\mathrm{T}}\dot{\boldsymbol{\varepsilon}}$ accounts for the mechanical work that contributes to the internal energy and therefore to the temperature evolution. This term embodies the mechanical-thermal coupling, linking strain variations to heat generation or absorption within the material. Together, these contributions ensure a fully coupled thermoelastic description, in which the temperature and strain fields are mutually dependent. Further details can be found in Refs. [21,27].

2.2. Finite element formulation

The Galerkin technique is utilized to obtain the FE formulation of Equations (7) and (8) [28]. In conventional FEM, the 3D domain within volume V can be discretized into a finite number of regular 3D solid elements. Therefore, the components of the displacement and temperature change in each element can be approximated by the shape functions as follows:

$$\mathbf{u}(x,y,z,t) = \phi_m(x,y,z)\mathbf{u}_m(t), \tag{9}$$

$$\mathrm{T}(x,y,z,t) = \phi_m(x,y,z)\Theta_m(t), \tag{10}$$

where $\mathbf{u}_m(t)$ and $\Theta_m(t)$ are the displacement vector and temperature change at each nodal point of the element, and $\phi_m(x,y,z)$ are the nodal shape functions of the element. The index m indicates the summation of the number of nodal points in the element.

According to the Galerkin method, multiplying both sides of Eqs.(7) and (8) by the shape functions ϕ_m and integrating over the volume of the element, yields the following:

$$\int (\nabla\cdot\boldsymbol{\sigma} + \mathbf{b} - \rho\ddot{\mathbf{u}})\phi_m dV = 0, \tag{11}$$

$$\int \left(\rho c_p \frac{\partial \mathrm{T}}{\partial t} - \nabla\cdot(\boldsymbol{\kappa}\nabla\mathrm{T}) + \mathrm{T}_0\boldsymbol{\beta}^{\mathrm{T}}\dot{\boldsymbol{\varepsilon}} - Q\right)\phi_m dV = 0. \tag{12}$$

Then, the divergence theorem can be applied to the first and second terms of Equations (11) and (12) as:

$$\int (\nabla\cdot\boldsymbol{\sigma})\phi_m dV = \int \boldsymbol{\sigma}\cdot\mathbf{n}\phi_m dS - \int \mathbf{D}^{\mathrm{T}}(\phi_m)\boldsymbol{\sigma} dV, \tag{13}$$

$$\int \nabla\cdot(\boldsymbol{\kappa}\nabla\mathrm{T})\phi_m dV = \int \boldsymbol{\kappa}\nabla\mathrm{T}\cdot\mathbf{n}\phi_m dS - \int \nabla\phi_m\boldsymbol{\kappa}\nabla\mathrm{T} dV. \tag{14}$$

Using the relationship between the traction vector acting $\mathbf{t}$ and the stress tensor, and the heat exchange occurring at an arbitrary surface of the body, the relation becomes:

$$\boldsymbol{\sigma}\cdot\mathbf{n} = \mathbf{t}, \tag{15}$$

$$-\boldsymbol{\kappa}\nabla\mathrm{T}\cdot\mathbf{n} = q_a + q_c + q_r, \tag{16}$$

in which q_a denotes an applied heat flux, and q_c and q_r are the convective and radiative heat fluxes, evaluated as follows:

$$q_c = h(\mathrm{T} - \mathrm{T}_\infty), \tag{17}$$

$$q_r = \sigma\varepsilon(\mathrm{T}^4 - \mathrm{T}_\infty^4), \tag{18}$$

where h and ε are the convective heat transfer coefficient and emissivity of the material, σ is the Stefan-Bolzmann constant, and T_∞ is the ambient temperature. The radiative heat flux introduces a nonlinear dependence on the temperature. To retain a linear finite element formulation, this term is linearized around a reference temperature T_0 using a first-order Taylor expansion, $\mathrm{T} = \mathrm{T}_0 + \Delta\mathrm{T}$. This leads to:

$$\mathrm{T}^4 = \mathrm{T}_0^4 + 4\mathrm{T}_0^3\Delta\mathrm{T} \tag{19}$$

Therefore, the radiative flux can be approximated as:

$$q_r = h_r(\mathrm{T} - \mathrm{T}_\infty), \quad h_r = 4\sigma\varepsilon\mathrm{T}_0^3 \tag{20}$$

where h_r acts as the effective radiative heat transfer coefficient. In this work, T_0 is chosen to be equal to the ambient temperature, which provides a sufficiently accurate approximation over the operating range considered and allows the radiative contribution to be incorporated in the same way as a convection boundary condition. Substituting Equations (13) to (16) into Equations (11) and (12) yields the following:

$$\int \rho\ddot{\mathbf{u}}\phi_m dV + \int \mathbf{D}^{\mathrm{T}}(\phi_m)\boldsymbol{\sigma} dV = \int \mathbf{b}\phi_m dV + \int \mathbf{t}\phi_m dS, \tag{21}$$

$$\int \rho c_p \frac{\partial \mathrm{T}}{\partial t}\phi_m dV + \int \nabla\phi_m \boldsymbol{\kappa}\nabla\mathrm{T} dV + \int \mathrm{T}_0\boldsymbol{\beta}^{\mathrm{T}}\mathbf{D}(\phi_m)\dot{\mathbf{u}} dV = \int Q\phi_m dV - \int (q_a + q_c + q_r)\phi_m dS. \tag{22}$$

Incorporating the convective and radiative heat fluxes into the latter equation, and adding the temperature-dependent terms to the left-hand side, leaves the following:

$$\begin{aligned}\int \rho c_p \frac{\partial \mathrm{T}}{\partial t}\phi_m dV + \int \nabla\phi_m \boldsymbol{\kappa}\nabla\mathrm{T} dV + \int \mathrm{T}_0\boldsymbol{\beta}^{\mathrm{T}}\mathbf{D}(\phi_m)\dot{\mathbf{u}} dV + \int h\phi_m \mathrm{T} dS + \int h_r\phi_m \mathrm{T} dS \\ = \int Q\phi_m dV - \int q_a\phi_m dS + \int h\phi_m \mathrm{T}_\infty dS + \int h_r\phi_m \mathrm{T}_\infty dS.\end{aligned} \tag{23}$$

2.3. Unified Formulation approach for the coupled thermo-elasticity problem

The Unified Formulation enables the discretization of a 3D solid using 1D finite elements (FEs) with 3D capabilities, incorporating a cross-sectional description of the field of displacements and temperature changes. The FE description utilizes the classical shape functions (N_i), whereas the cross-section is characterized by the expansion functions F_τ. In this regard, the displacement and temperature fields can be posed as follows:

$$\begin{aligned}\mathbf{u} &= N_i\mathbf{u}_i = N_iF_\tau\mathbf{u}_{\tau i}, \\ T &= N_i\mathrm{T}_i = N_iF_\tau\Theta_{\tau i},\end{aligned} \tag{24}$$

where $i = 1, \ldots, N_n$ and $\tau = 1, \ldots, M$ denote summation on the number of nodes (N_n) within each FE and the expansion function terms. For the sake of clarity, the Cartesian representation in the case of 1D beam FEs is illustrated in Figure 1.

For the sake of conciseness, Equations (21) and (23) are written in terms of the FE shape functions and expansion functions, regardless of the FE model chosen. The reader is invited to consult [20] to explore in more detail how the volume integral can be decomposed into beam and cross-sectional integrals in the context of 1D models. Similarly, the Galerkin shape function ϕ_m can be written as:

$$\phi_m = N_jF_s. \tag{25}$$

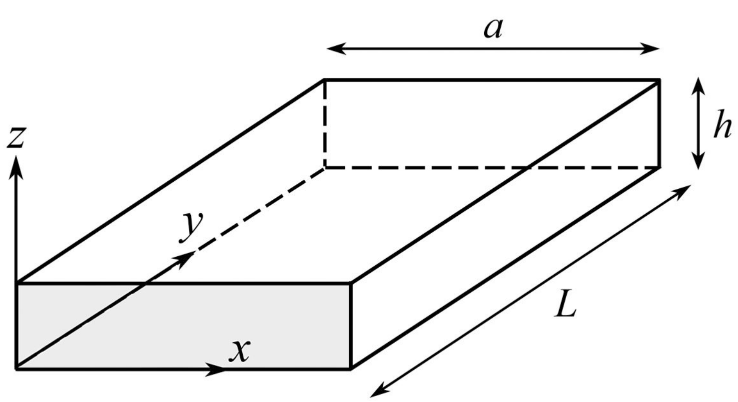

Figure 1. Beam model geometry and reference system representation.

Equations (24) and (25) can be substituted into Equations (21) and (23) to give:

$$\int \rho N_i N_j F_\tau F_s \ddot{\mathbf{u}}_{\tau i} dV + \int \mathbf{D}^T (N_j F_s) \mathbf{C} \mathbf{D} (N_i F_\tau) \mathbf{u}_{\tau i} dV = \int \mathbf{b} N_j F_s dV + \int \mathbf{t} N_j F_s dS \tag{26}$$

$$\begin{aligned} &\int \rho c_p N_i N_j F_\tau F_s \dot{\Theta}_{\tau i} dV + \int \nabla (N_j F_s) \boldsymbol{\kappa} \nabla (N_i F_\tau) \Theta_{\tau i} dV + \int \mathrm{T}_0 \boldsymbol{\beta}^T \mathbf{D} (N_j F_s) N_i F_\tau \dot{\mathbf{u}}_{\tau i} dV \\ &+ \int h N_i N_j F_\tau F_s \Theta_{\tau i} dS + \int h_r N_j F_s (N_i F_\tau \Theta_{\tau i}) dS \\ &= \int Q N_j F_s dV - \int q_a N_j F_s dS + \int h N_j F_s \mathrm{T}_\infty dS + \int h_r N_j F_s \mathrm{T}_\infty dS. \end{aligned} \tag{27}$$

The presented approach enables all the FE matrices and vectors to be derived as a condensed notation, referred to as Fundamental Nucleus (FN). For the coupled formulations, the FNs are 4×4 matrices or 4×1 vectors. For clarity, all FNs share the same integral structure. Each FN block results from the combination of: (i) the axial FE shape functions, (ii) the cross-sectional expansion functions, and (iii) the corresponding material tensor. This separation between axial and cross-sectional integrals ensures dimensional consistency among all FN terms and highlights their interdependence. In particular, the mechanical stiffness, thermal conductivity, and thermo-elastic coupling matrices are derived from analogous operators acting on different physical quantities, a key feature of the Unified Formulation. This unified structure allows the same FN definitions to be reused for any choice of structural theory.

Accordingly, Equations (26) and (27) can be rewritten in matrix form in the static case as follows:

$$\begin{bmatrix} \mathbf{m}_{uu}^{ij\tau s} & 0 \\ 0 & 0 \end{bmatrix} \begin{Bmatrix} \ddot{\mathbf{u}}_{\tau i} \\ \ddot{\Theta}_{\tau i} \end{Bmatrix} + \begin{bmatrix} 0 & 0 \\ \mathbf{g}_{\Theta u}^{ij\tau s} & \mathbf{g}_{\Theta\Theta}^{ij\tau s} \end{bmatrix} \begin{Bmatrix} \dot{\mathbf{u}}_{\tau i} \\ \dot{\Theta}_{\tau i} \end{Bmatrix} + \begin{bmatrix} \mathbf{k}_{uu}^{ij\tau s} & \mathbf{k}_{u\Theta}^{ij\tau s} \\ 0 & \mathbf{k}_{\Theta\Theta}^{ij\tau s} \end{bmatrix} \begin{Bmatrix} \mathbf{u}_{\tau i} \\ \Theta_{\tau i} \end{Bmatrix} = \begin{Bmatrix} \mathbf{f}^{js} \\ q^{js} \end{Bmatrix}, \tag{28}$$

where the FN of the stiffness matrix, load, and flux vectors can be expressed as:

$$\mathbf{m}_{uu}^{ij\tau s} = \int \rho N_i N_j F_\tau F_s dV, \tag{29}$$

$$\mathbf{g}_{\Theta u}^{ij\tau s} = \int \mathrm{T}_0 \boldsymbol{\beta}^{\mathrm{T}} \mathbf{D} (N_j F_s) N_i F_\tau dV, \mathbf{g}_{\Theta\Theta}^{ij\tau s} = \int \rho c_p N_i N_j F_\tau F_s dV, \tag{30}$$

$$\mathbf{k}_{uu}^{ij\tau s} = \int \mathbf{D}^{\mathrm{T}} (N_j F_s) \mathbf{C} \mathbf{D} (N_i F_\tau) dV, \mathbf{k}_{u\Theta}^{ij\tau s} = -\int \mathbf{D}^{\mathrm{T}} (N_j F_s) \boldsymbol{\beta} N_i F_\tau dV, \tag{31}$$

$$\mathbf{k}_{\Theta\Theta}^{ij\tau s} = \int \nabla(N_j F_s)\boldsymbol{\kappa}\nabla(N_i F_\tau)dV + \int hN_iN_jF_\tau F_s\Theta_{\tau i}dS + \int h_r N_j F_s(N_i F_\tau \Theta_{\tau i})dS, \tag{32}$$

$$\mathbf{f}^{js} = \int \mathbf{b}N_j F_s dV + \int \mathbf{t}N_j F_s dS, \tag{33}$$

$$q^{js} = \int QN_jF_sdV - \int q_a N_j F_s dS + \int hN_jF_s\mathrm{T}_\infty dS + \int h_r N_j F_s \mathrm{T}_\infty dS. \tag{34}$$

Subsequently, the mass, damping, and stiffness matrices, as well as the force and flux vectors of the whole structure, can be assembled by looping through the τ and s expansion function indices, and then through the i and j FE indices, leading to:

$$\mathbf{M}\,\ddot{\mathbf{q}} + \mathbf{G}\dot{\mathbf{q}} + \mathbf{K}\mathbf{q} = \mathbf{P}, \tag{35}$$

where $\mathbf{M}$, $\mathbf{G}$, and $\mathbf{K}$ are the mass, damping, and stiffness matrices, while $\mathbf{q}$ is the vector containing the unknowns of both displacements and temperature. Similarly, $\mathbf{P}$ is the global vector of the applied mechanical and thermal loads. Finally, to solve the time domain response, the Newmark method [29] is adopted. For brevity, readers are referred to Refs. [30,31] for the detailed procedure.

3. Numerical examples

This section evaluates various structures under different thermal conditions to demonstrate the accuracy and capabilities of the presented coupled thermo-elastic methodology. Conduction and convection analyses were performed on both external and embedded electronic devices, comparing the results with solutions from 3D solid models. Each case study highlights two key aspects: (i) the impact of the structural theories used and (ii) the significant reduction in computational cost achieved by employing the presented beam models over solid solutions from commercial software.

3.1. Aluminum panel under thermal loadings

The first assessment involves the thermo-mechanical response of a clamped aluminum panel subjected to a uniform heat flux. This structure, depicted in Figure 2, has the following material properties: Young's modulus $E = 70\,\mathrm{GPa}$, Poisson's ratio $\nu = 0.3$, coefficient of thermal expansion $\alpha = 23\times10^{-6}\ \mathrm{K}^{-1}$, and thermal conductivity $\kappa = 235\,\mathrm{W/(m\ K)}$. A heat flux of $q = 1000\,\mathrm{W/m^2}$ is applied to the panel, and the temperature at the clamped edge is set to $\mathrm{T}_0 = 0^\circ\mathrm{C}$.

To ensure accurate results, convergence studies, reported in Figures 3 and 4, were performed to evaluate the effects of mesh approximation and structural theories adopted in the beam cross-section. First, the influence of mesh density along the y-axis was examined using various B4 elements, while 16LE9 were used for the $x - z$ discretization. Figure 3 shows that one B4 element is sufficient to accurately capture the temperature trend along the longitudinal axis. However, at least four B4 elements are required to correctly represent the stress distribution. Then, with the y-axis finite element discretization fixed, the effect of different kinematic theories on the beam cross-section was assessed. Figure 4 provides the axial displacement and normal stress along the y-axis and through-the-thickness. The results clearly prove that classical theory (i.e., TE1) cannot capture the correct thermo-mechanical response of this structure. Higher-order theories, such as 16LE9 (4420 DOFS) or TE5 (1092 DOFs), are necessary to accurately predict both displacement and stress distributions. Consequently, the convergent model was achieved using four B4 beam elements along the longitudinal axis combined with either 16L9 or TE5 for the cross-section

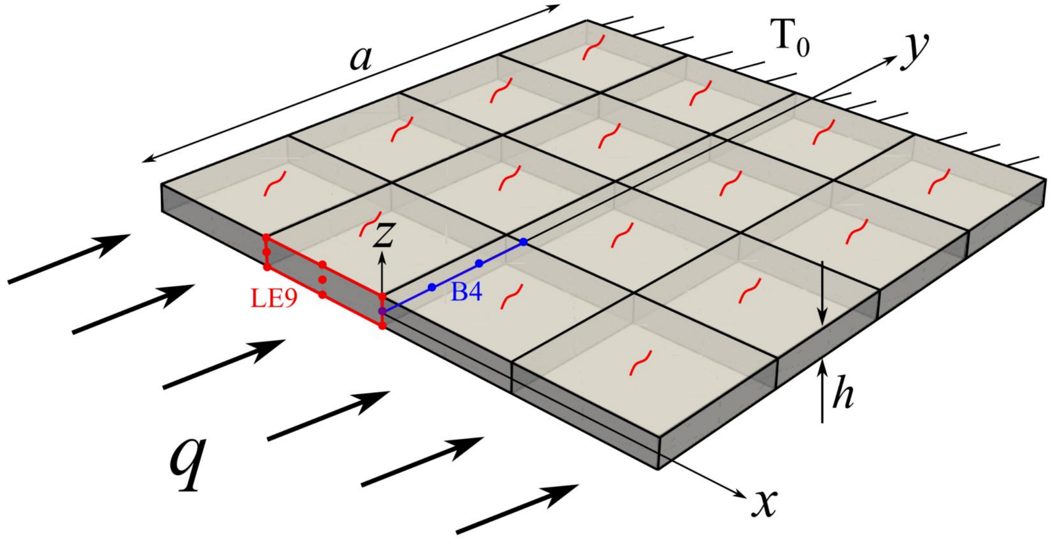

Figure 2. Geometric representation and discretization of the FE model of the aluminum panel.

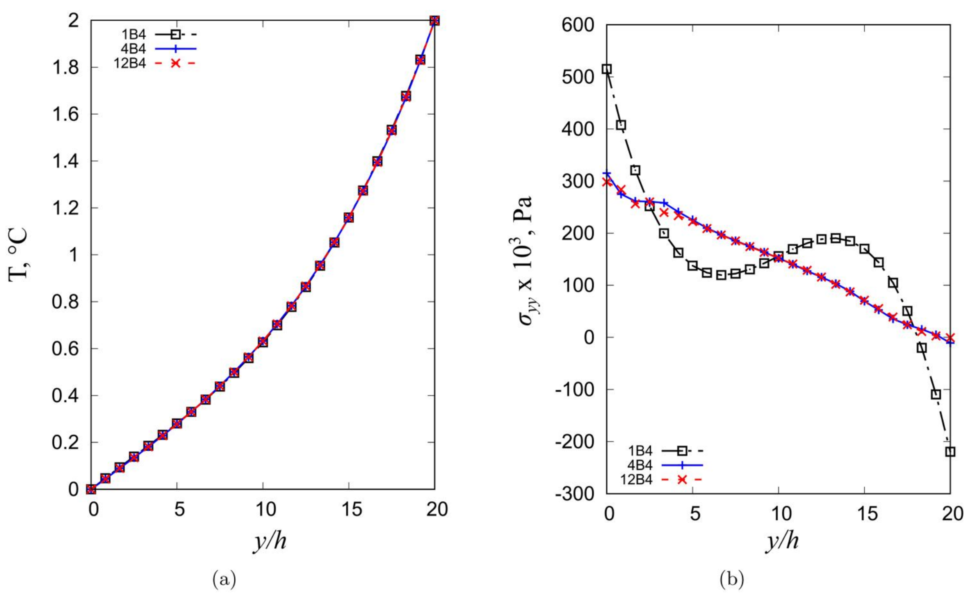

Figure 3. Mesh convergence study for the aluminum panel. Temperature and axial stress along the y/h ratio.

discretization. For all subsequent analyses, the 4B4 + TE5 model was adopted due to its balance of accuracy and computational efficiency.

Figure 5 illustrates the axial displacement, temperature, normal and shear stress distributions as functions of the y or z coordinates. This figure also includes a comparison between cases with and without convection, and a validation against a 3D Abaqus (ABQ) solution (1800 C3D8T elements). Furthermore, the deformed configurations showing the displacement and temperature contours based on the CUF 1D model (4B4 + TE5) are depicted in Figures 5a and 5b, respectively.

The results show that the CUF results exhibit excellent agreement with the Abaqus solid solutions, for both convective and non-convective scenarios. This agreement is achieved with a

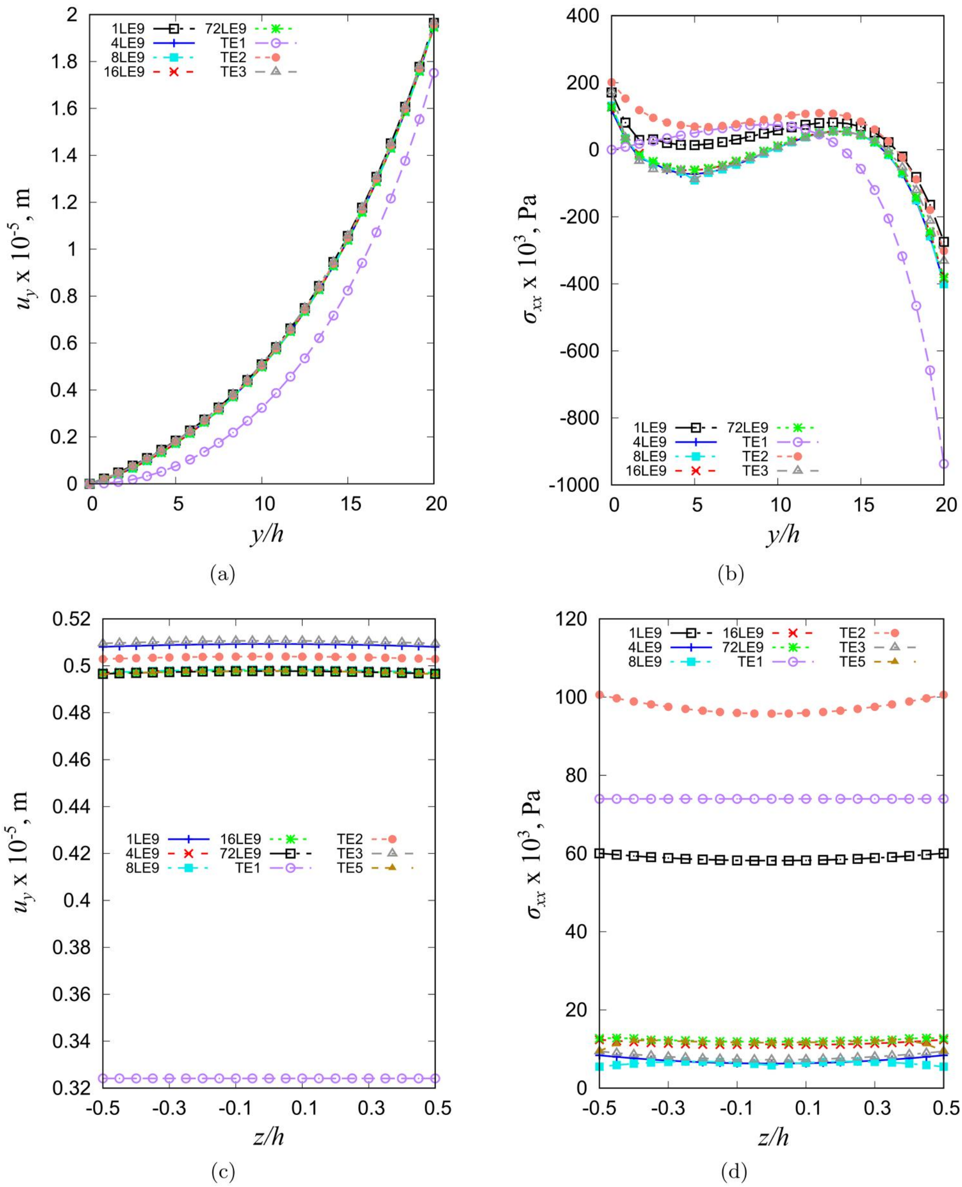

Figure 4. Effect of the structural theory for the aluminum panel.

significant reduction in the degree of freedom compared to the convergent 3D Abaqus model, highlighting the computational efficiency of the CUF approach. This initial case successfully demonstrates the efficacy of different structural theories and serves as a crucial validation for the methodology.

3.2. Flexible electronic device with external chip

The second example concerns a polydimethylsiloxane (PDMS) substrate layer and an aluminum oxide (AlO) chip. The substrate has geometrical characteristics of $a = 30\,\text{mm}$, $h_S = 3\,\text{mm}$. The $4\times2\times0.5\,\text{mm}$ chip, centrally located on the substrate's top surface, is the functional component and generates heat solely through the Joule effect, contributing to the model's heat source.

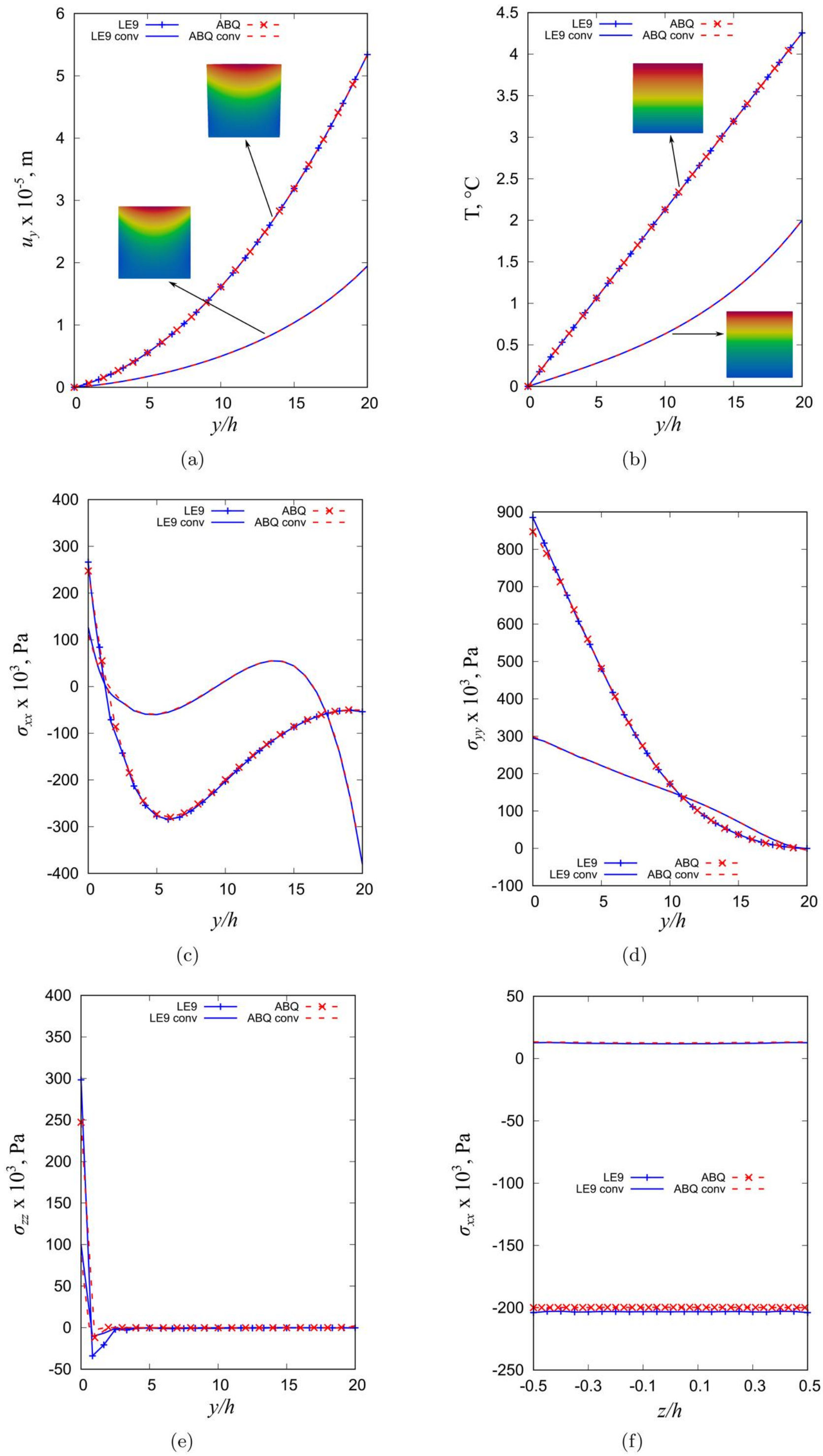

Figure 5. Comparison of present methodology with 3D abaqus solutions for the aluminum panel, considering scenarios with and without convection.

Table 1. Material properties of the FED with external chip.

Material	Young Modulus [MPa]	Poisson ratio	Density [kg/m^3]	Thermal expansion coefficient [K^{-1}]	Specific heat [J/kg K]	Conductivity [W/(m K)]
PDMS	1.80	0.49	970	2.5×10^{-6}	1459.79	0.15
AlO	285000	0.30	3990	8.5×10^{-6}	179.95	30

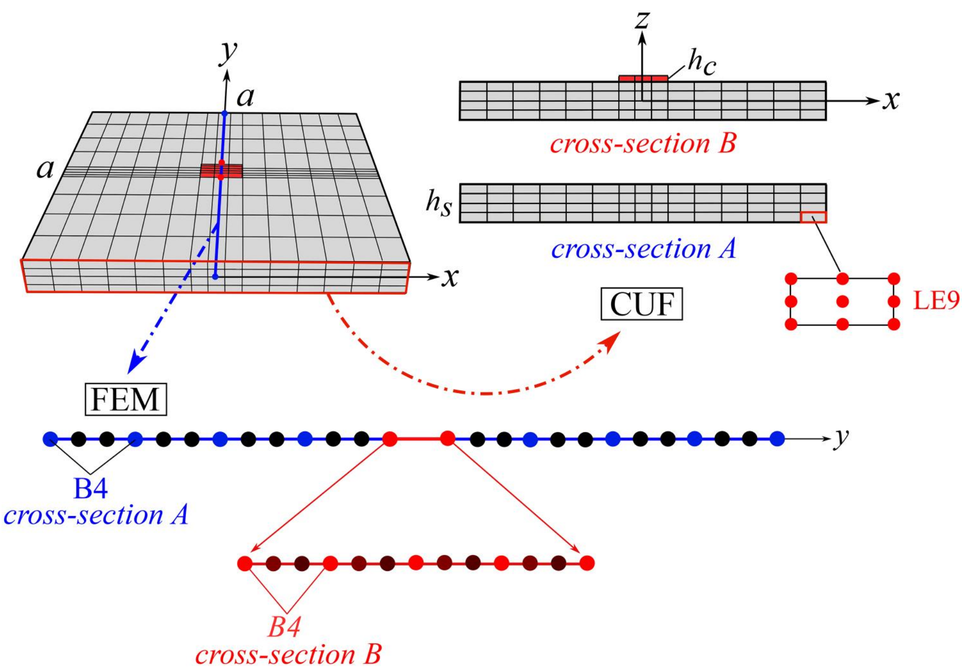

Figure 6. Geometric representation and discretization of the FE model of the FED with external chip.

Table 1 provides the material properties for both components. The structure is clamped at its bottom surface, which is maintained at an ambient temperature of 26°C. The functional component generates a constant heat flux $q = 0.291$ W. Convection at the top surface is characterized by a coefficient of 25 W/(m^2 K).

The structural component was modeled utilizing both lower-order and higher-order beam formulations. Specifically, various B4 finite elements were adopted along the y-axis, while TE and LE theories were applied within the $x-z$ plane. Figure 6 illustrates the reference system and the geometrical features of the component, detailing its modeling in both the FEM and CUF frameworks.

The convergence analysis for the mesh approximation along the y-axis is provided in Table 2, while the study concerning the kinematic expansion is given in Table 3. The results are evaluated at the center of the chip's top surface. Both scenarios, with and without convection, are examined, and the results are compared with the Abaqus solid model for validation purposes.

The results indicate that employing 12B4 finite elements along the y-axis and $60+3$ L9 over the cross-section yields a robust and accurate discretization of the structural component. Moreover, the comparative analysis with the Abaqus solid solution demonstrates good agreement in the results, accompanied by a significant reduction in the computational cost, equal to approximately 90.65%, highlighting the efficiency of the proposed 1D modeling approach. Considering an equivalent number of degrees of freedom, the Abaqus solid model presents an error of about 10% in temperature and 5% in displacement for the convection case. Figure 7 illustrates the

Table 2. Convergence analysis on mesh approximation for the FED with external chip. Model with 60 L9 in the substrate and 3 L9 in the functional component (60 + 3 L9). The number of the total degrees of freedom (DOFs) is reported in brackets.

	convection		no convection	
Model	u_z [mm]	T [°C]	u_z [mm]	T [°C]
3B4 (11384)	0.159	190.70	0.165	198.72
6B4 (21596)	0.159	212.98	0.165	219.37
9B4 (31808)	0.159	218.65	0.165	226.54
12B4 (42020)	0.159	222.20	0.165	231.03
15B4 (52232)	0.159	223.17	0.166	232.02

Table 3. Effect of the kinematic theories on the transverse displacement and temperature for the FED with external chip. Model with 12B4 FEs. The number of the total degrees of freedom (DOFs) is reported in brackets.

	convection		no convection	
Model	u_z [mm]	T [°C]	u_z [mm]	T [°C]
20 + 2 L9 (16060)	0.165	216.28	0.171	223.56
60 + 3 L9 (42020)	0.159	222.20	0.165	231.03
100 + 4 L9 (67684)	0.159	223.14	0.165	232.43
3D ABQ (41512)	0.147	202.22	0.162	223.54
3D ABQ (449696)	0.154	222.95	0.166	236.39

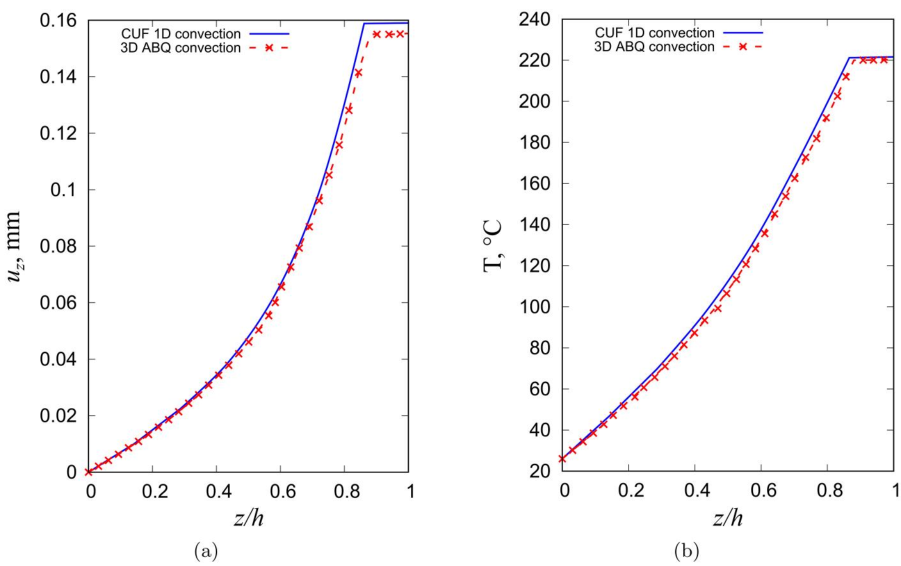

Figure 7. Through-the-thickness transverse displacement and temperature distributions at the center of the chip's top surface for the FED with external chip. 12B4 + 60 + 3 LE9 model.

transverse displacement and temperature distribution along the thickness. The deformed configurations and temperature contours are depicted in Figure 8, highlighting the comparison between the mesh approximations adopted in the CUF and 3D Abaqus models.

3.3. Flexible electronic device with embedded chip

The next case deals with a flexible electronic device with an embedded chip. This structural component contains a rectangular functional component, a substrate layer and an encapsulated layer, see Figure 9. In this figure, the embedded chip, substrate layer, and encapsulated layer have the length, width and thickness expressed as l_{fc}, b_{fc}, h_{fc}, l_{sl}, b_{sl}, h_{sl}, and l_{el}, b_{el}, h_{el}, respectively. The total thickness is equal to $h = 3\,\text{mm}$. The geometric and material characteristics are given in

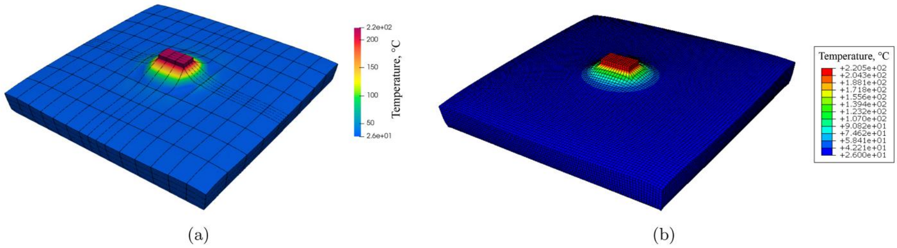

Figure 8. Comparison of temperature contours for the FED with external chip. (a) 1D CUF 12B4 + 60 + 3 LE9 model; (b) 3D abaqus 100172 C3D8T model. The deformations have been magnified by a factor equal to 15.

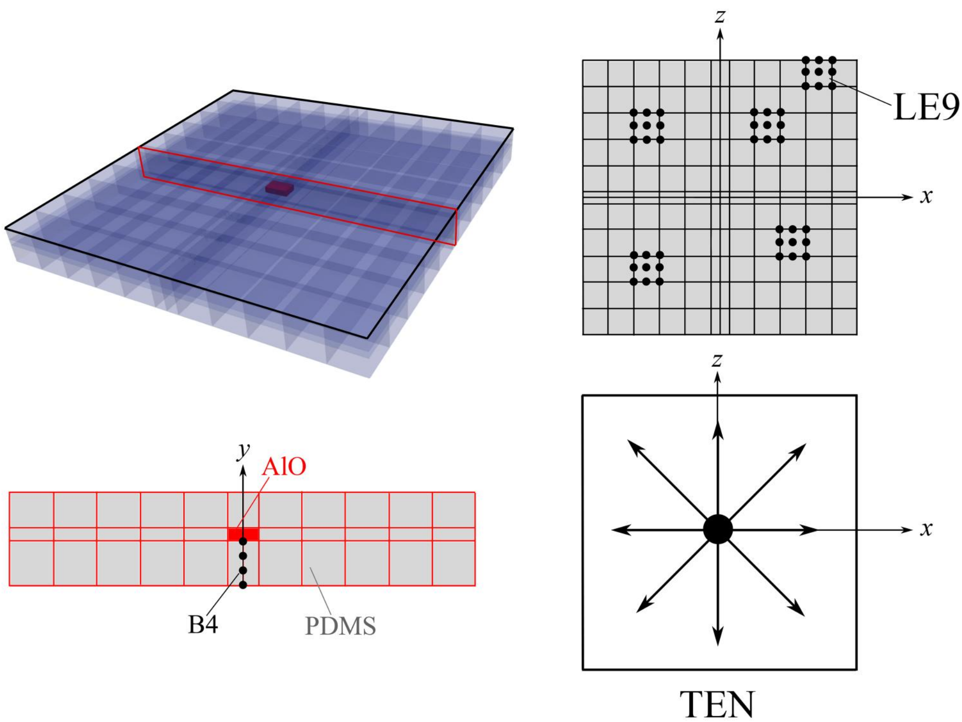

Figure 9. Geometric representation and discretization of the FE model of the FED with embedded chip.

Table 4. Geometric and material characteristics of the FED with embedded chip.

Functional component				Substrate layer				Encapsulated layer			
l_{fc} [mm]	b_{fc} [mm]	h_{fc} [mm]	Material	l_{sl} [mm]	b_{sl} [mm]	h_{sl} [mm]	Material	l_{el} [mm]	b_{el} [mm]	h_{el} [mm]	Material
2.0	1.25	0.5	AlO	**30.0**	30.0	1.5	PDMS	**30.0**	30.0	1.0	PDMS

Table 4. The structure is clamped at its bottom surface, which is maintained at an ambient temperature of 26°C. The internal chip generates a constant heat flux $q = 0.291$ W. Convection at the top surface is characterized by a coefficient of 25 W/(m^2 K).

Table 5 provides the convergence analysis of mesh approximation along the y-axis for both the displacement and temperature, whereas the effect of the kinematic expansion is given in Table 6. All results are evaluated at the center of the device's top surface. To validate the proposed model, results are compared against 3D simulations performed using Abaqus.

The results suggest that a discretization using 6B4 elements along the beam axis and 576 L9 over the cross-section yields a convergent model. Moreover, comparison with the Abaqus solid

Table 5. Convergence study on mesh approximation for the FED with embedded chip. Model with 576 L9 (3×3 L9 in the chip). The number of the DOFs is reported in brackets.

Model	u_z [mm]	T [°C]
3B4 (96040)	0.141	128.26
6B4 (182476)	0.139	128.41
12B4 (355348)	0.139	128.41

Table 6. Effect of the kinematic theories on the transverse displacement and temperature for the FED with embedded chip. Model with 6B4 FEs. The number of the DOFs is reported in brackets.

Model	u_z [mm]	T [°C]
144 L9 (47500)	0.129	126.39
289 L9 (93100)	0.134	127.64
576 L9 (182476)	0.139	128.41
696 L9 (2189716)	0.139	128.41
TE1 (228)	0.048	28.43
TE2 (456)	0.056	33.30
TE3 (760)	0.057	33.31
TE5 (1596)	0.065	39.86
TE8 (3420)	0.087	56.31
TE12 (6916)	0.088	61.67
3D ABQ (155024)	0.125	117.29
3D ABQ (3604212)	0.143	128.39

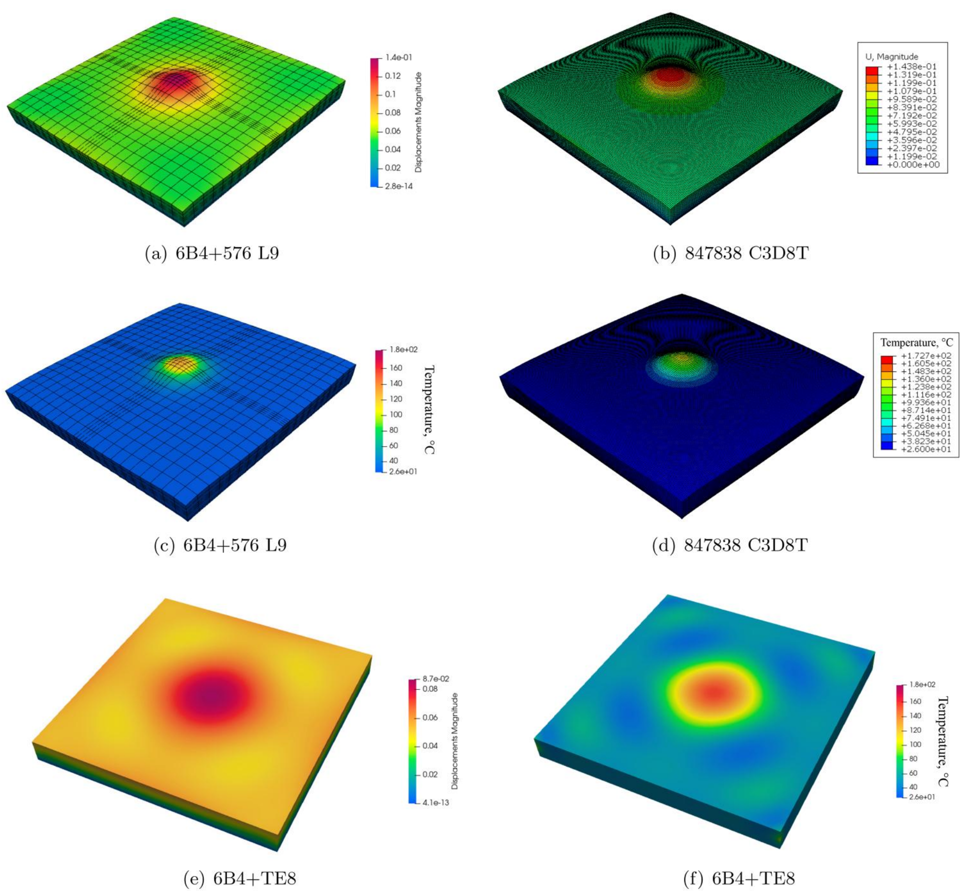

(a) 6B4+576 L9 (b) 847838 C3D8T

(c) 6B4+576 L9 (d) 847838 C3D8T

(e) 6B4+TE8 (f) 6B4+TE8

Figure 10. Displacement and temperature contours for the FED with embedded chip. Comparison between the 1D CUF LE9 model (a,c), 3D abaqus (b, d), and TE8 solutions (e, f). The deformations have been magnified by a factor equal to 15.

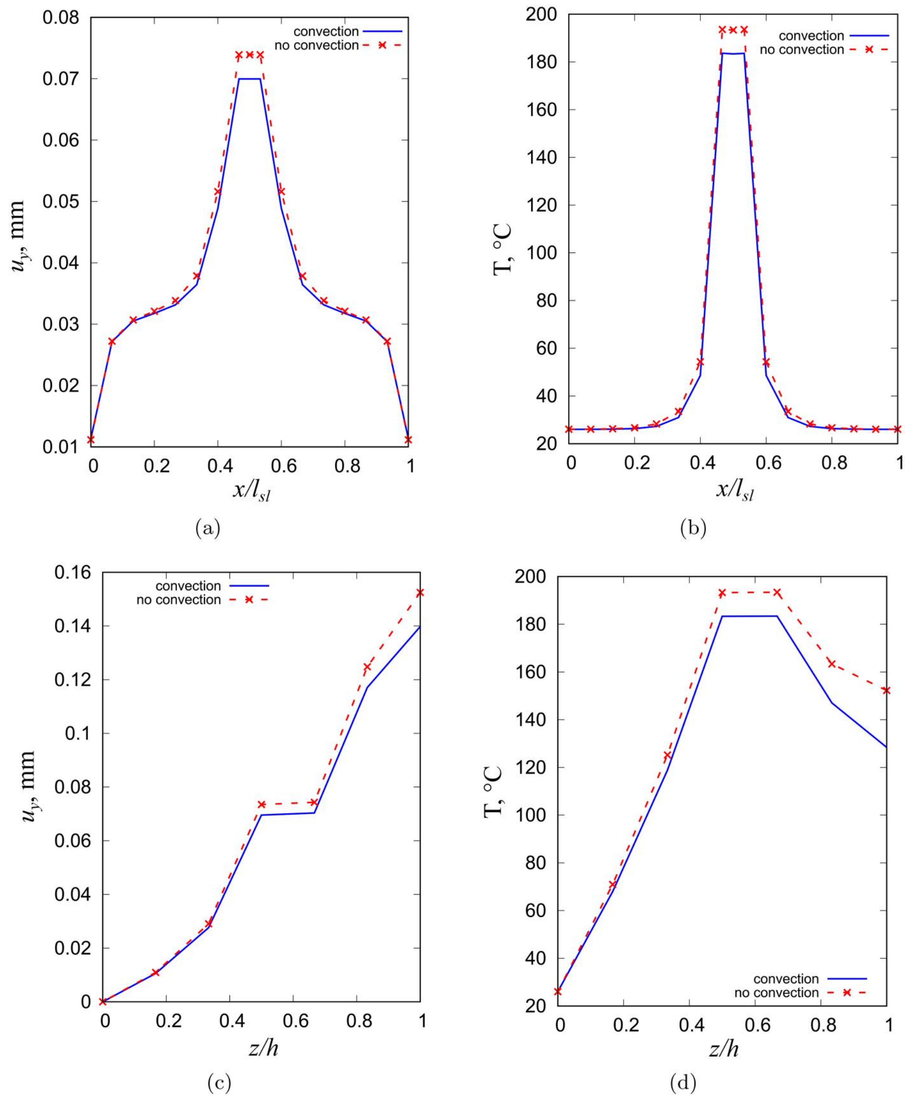

Figure 11. Displacement and temperature distributions along the *x*- and *z*-direction for the FED with embedded chip. Comparison between the scenario with and without convection.

model reveals a significant reduction in computational cost. Specifically, the CUF-based approach achieves approximately a 95% reduction in DOFs compared to the converged Abaqus 3D model (3604212 DOFs, 847838 C3D8T elements). In the literature, a 3D approach is often adopted to address these problems, primarily due to the pronounced local effects caused by localized thermal loads. Such cases require thorough and precise FE models. A parallel can be drawn with the well-known Meyer-Piening study [32], which investigated the impact of localized pressure loads. The main advantage of the proposed 1D methodology lies in its ability to achieve the same level of accuracy as highly refined 3D models, while significantly reducing computational costs. In addition, the results highlight the necessity of employing Lagrange theory to obtain accurate solutions. In contrast, Taylor models fail to capture the localized effects of thermal variations, resulting in significant inaccuracies, even when higher-order polynomial expansions are used. A degree of convergence in deflection is observed

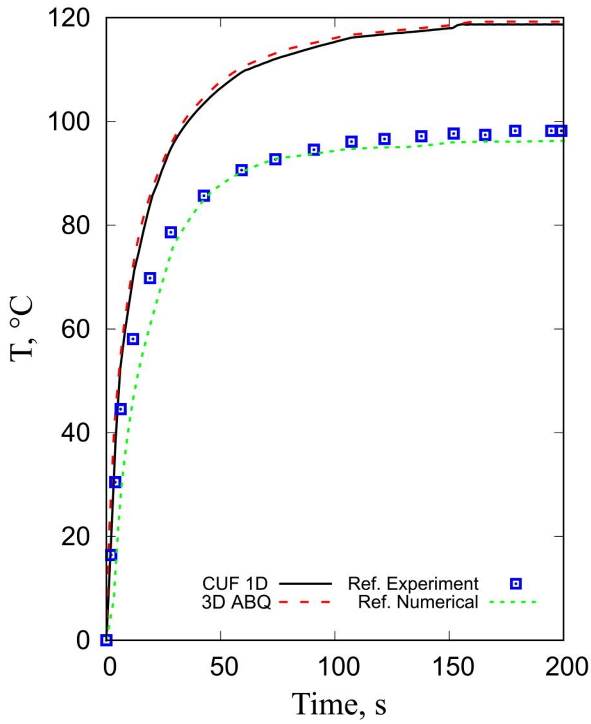

Figure 12. Temperature variation over time in the FED incorporating an embedded chip. Comparison between the proposed method, 3D abaqus simulation, and experimental and numerical reference data [33].

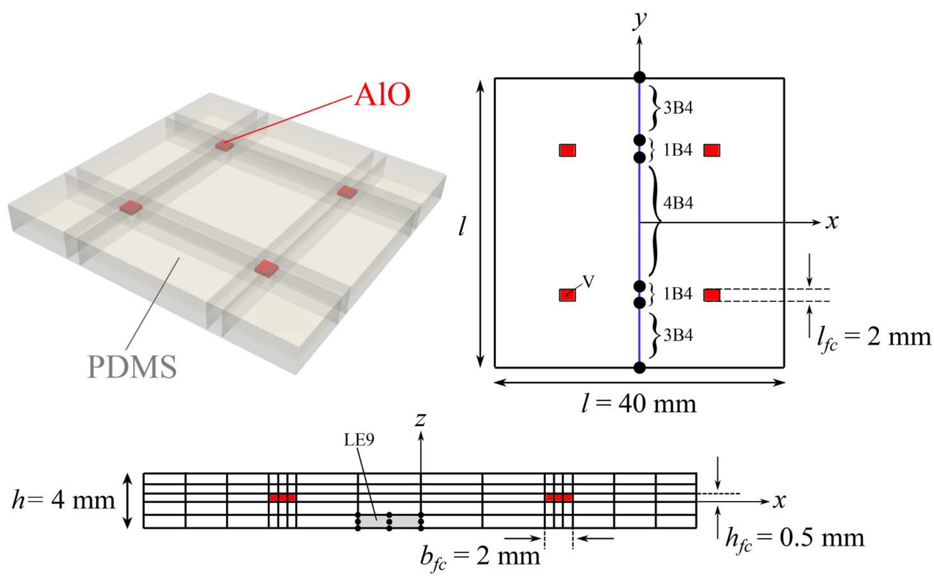

Figure 13. Reference system, geometric representation and FE discretization of the structural component with multiple embedded functional component.

between TE8 and TE12. However, the predicted temperature continues to increase. This suggests that a significantly higher-order TE would be required to reach the values predicted by LE models. In fact, a 68th-order expansion would be necessary to match the number of DOFs of the 576 L9 model, with

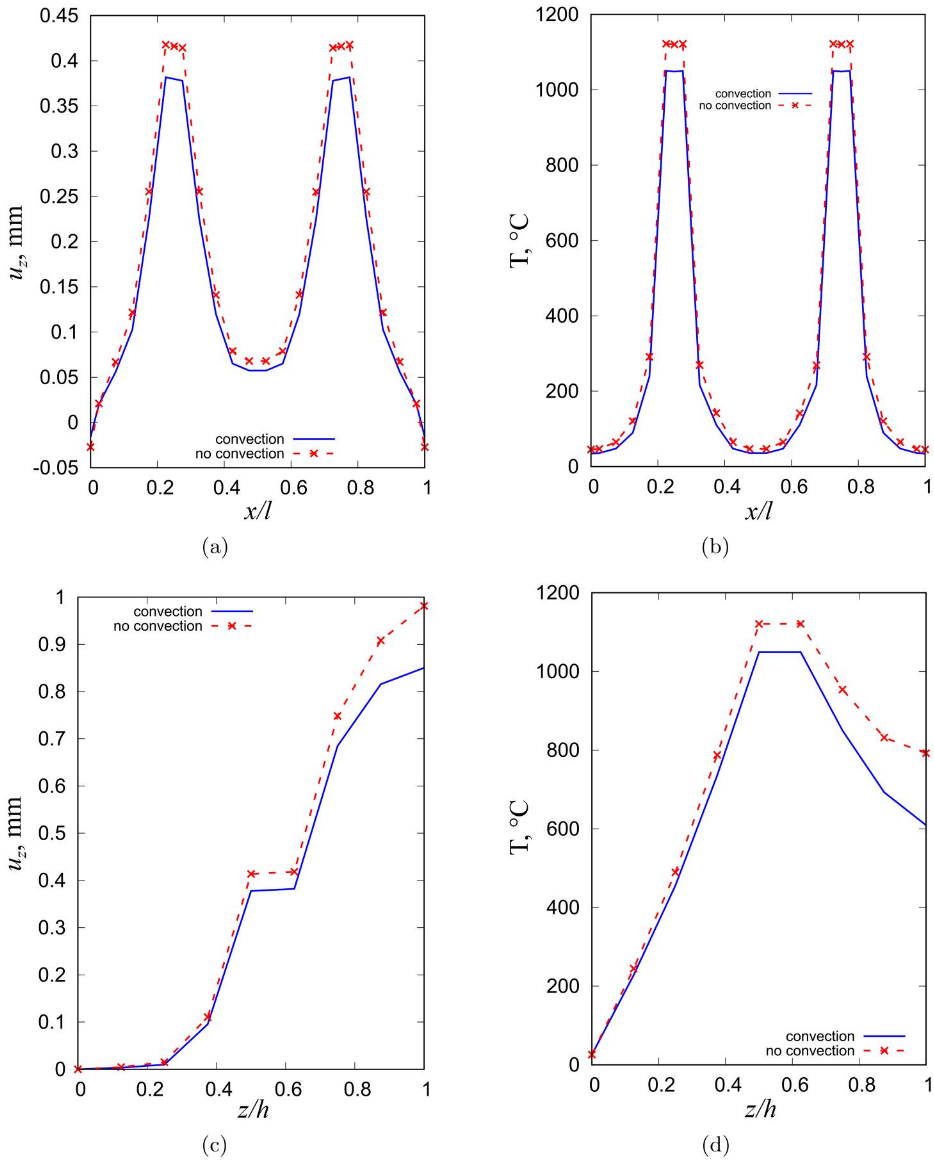

Figure 14. Displacement and temperature distributions along the *x*- and *z*-direction for the structural component with multiple embedded chips. Comparison between the scenario with and without convection.

no guarantee that the resulting fields would align with the LE and 3D Abaqus solutions. Figure 10 shows the deformed configurations of the CUF 1D LE9 and TE8 models, as well as the 3D Abaqus solid solution, with both displacement and temperature contours illustrated.

Figure 11 depicts the axial displacement and temperature trends at the midpoint of the structural component with the embedded functional component, plotted along both the length and thickness of the FED.

The results show a reduction ranging approximately from 5% to 8% in the axial displacement and from 5% to 16% in temperature when considering convection compared to the case without convection along the *x*- and *z*-direction, respectively.

Next, the dynamic thermal response of this electronic device is examined. Figure 12 illustrates the temperature variation over time at the coordinate (0.5 mm, 14.5 mm, 3 mm), comparing the

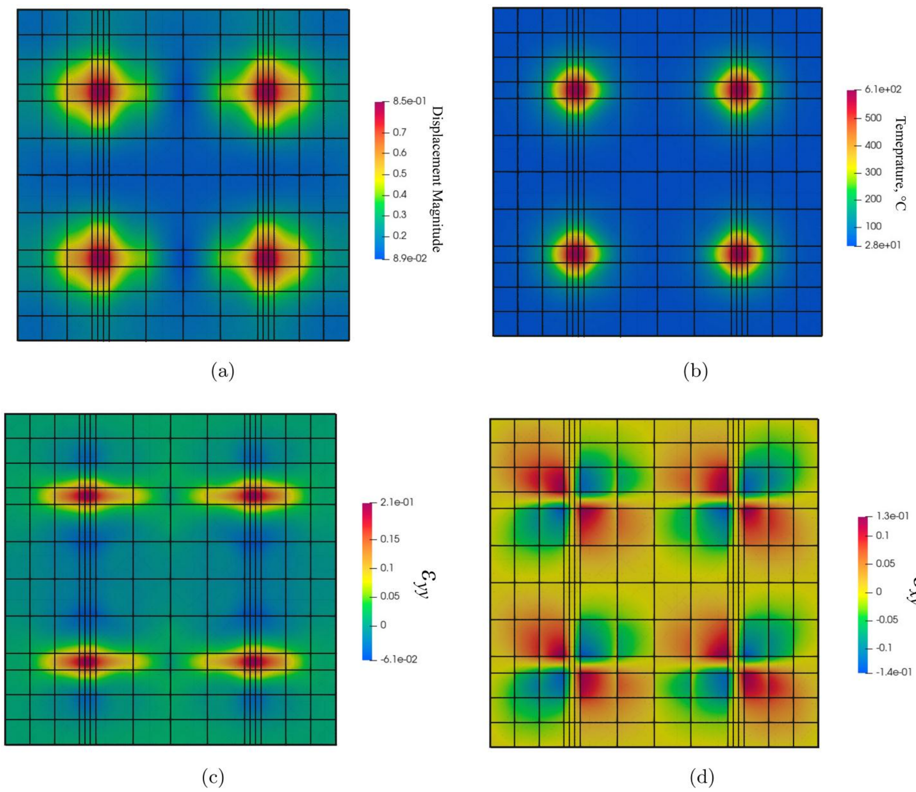

Figure 15. Displacement, temperature, strain in *y*-direction and shear strain contours at the top surface of the structural component with multiple embedded chips. Case with convection.

Table 7. Summary of accuracy and computational efficiency for all case studies.

Case study	CUF 1D DOFs	3D ABQ DOFs	DOFs reduction [%]	Displacement [%]	Temperature [%]
Aluminum panel	1092	11532	90.50	< 3	< 2
FED with external chip	42020	449696	90.65	< 4	< 3
FED with embedded chip	182476	3604212	94.94	< 3	< 1

results obtained from the present approach with those from a 3D Abaqus simulation, as well as with experimental and numerical reference data from Zhang *et al.* [33]. The results demonstrate a strong correlation between the proposed method and the 3D solid model, whereas noticeable discrepancies arise when compared to the reference solutions. These differences are attributed to variations in geometric and material properties between the current model and those used in the reference literature.

Finally, a structural component incorporating multiple embedded chips is analyzed. Figure 13 illustrates the device, detailing the reference coordinate system, geometric characteristics, and the FE model employed. The convergent model was achieved employing 12B4 elements along the beam axis and 80 L9 across the cross-section.

Figure 14 shows the transverse displacement and temperature variation at point V, plotted along both the longitudinal and thickness directions of the structural component with multiple embedded chips.

Furthermore, the contours of the strain in the *y*-direction, shear strain, displacement and temperature on the top of the considered structural component are shown in Figure 15. Higher-order TE structural models were not considered, as the single-chip configuration demonstrated their inability to accurately predict displacement and temperature fields. Notably, a linear relationship with the number of embedded chips is found between the peak temperature values in the single- and multi-chip cases. In the multi-chip case, the temperature contour displayed in Figure 15b reaches a peak of 610°C, whereas in the single-chip case, this maximum value is approximately 180°C. Similarly, the temperature distribution plots in Figures 11b, 11d and Figures 14b, 14d show maximum values of around 180°C and 1000°C for the single- and multi-chip configurations, respectively.

4. Conclusions

This work presents a robust and efficient methodology for analyzing the coupled thermo-elastic behavior of flexible electronic devices using refined one-dimensional (1D) beam models based on the Carrera Unified Formulation (CUF). The proposed approach successfully captures thermal and mechanical interactions while significantly reducing computational cost compared to traditional three-dimensional (3D) solid models, without compromising accuracy. The results show that using refined 1D beam models based on CUF allows the accurate evaluation of displacements, temperature variations, and stress distributions for structures subjected to different heat fluxes. Different Taylor expansions (TE) and Lagrange polynomial expansions (LE) have been compared, highlighting the ability of this methodology to easily build more complex models, such as a flexible electronic device with internal or external chips, including convection effects. Specifically, LE models are essential for accurately capturing localized thermal effects generated by electronic devices, effects that even high-order TE theories fail to evaluate reliably. A comparison of CUF 1D models based on LE theories with full 3D solid models reveals computational savings exceeding 90%. For completeness, a concise overview of the results is provided in Table 7. Overall, the findings highlight the potential of this modeling strategy for various phases of the design process of flexible electronic components. Future research will extend the framework to more intricate geometries, such as serpentine patterns, rotating components, and multi-body systems, and incorporate nonlinearities to further enhance its predictive capabilities. Furthermore, novel FE basis as those depicted in [34,35] can be explored to better account for local stress and temperature gradients.

Disclosure statement

No potential conflict of interest was reported by the author(s).

References

[1] Y. Feng and L. Wu, "Analysis of interfacial thermal stresses of chip-substrate structure," *Int. J. Solids Structures*, vol. 38, no. 9, pp. 1551–1562, 2001. DOI: 10.1016/S0020-7683(00)00099-8.
[2] L. Wu, "The thermoelastic analysis of chip-substrate system," *J. Electron. Packag.*, vol. 126, no. 3, pp. 325–332, 2004. DOI: 10.1115/1.1772413.
[3] M. Quirino, G. D'Anna, M. Guilizzoni, L. Marocco, F. Piscaglia and M. Lavagna, "Validation of the thermal model for the HERMES cubesat payload and evaluation of the performance of newly designed passive thermal links," *Aerotec. Missili. Spaz.*, pp. 1–23, 2025. DOI: 10.1007/s42496-025-00287-z.
[4] P. M. Jeyaraj, S. K. Biswal, S. B. Sudhakaran, T. Kurian and S. Thandavarayan, "Thermo-structural assessment of un-submerged flex nozzle system with 4D carbon–carbon nozzle liner," *Aerotec. Missili. Spaz.*, pp. 1–20, 2025. DOI: 10.1007/s42496-025-00262-8.
[5] J. H. Lim, M. Han, J. Y. Lee, Y. Y. Earmme, S. Lee and S. Im, "A study on the thermomechanical behavior of semiconductor chips on thin silicon substrate," *J Mech. Sci Technol.*, vol. 22, no. 8, pp. 1483–1489, 2008. DOI: 10.1007/s12206-008-0502-x.
[6] D. H. Kim, *et al.*, "Epidermal electronics," *Sci.*, vol. 333, no. 6044, pp. 838–843, 2011. DOI: 10.1126/science.1206157.

[7] J. W. Lee, *et al.*, “Soft, thin skin-mounted power management systems and their use in wireless thermography,” *Proc Natl Acad Sci U S A*, vol. 113, no. 22, pp. 6131–6136, 2016. DOI: 10.1073/pnas.1605720113.

[8] H. Lee, *et al.*, “A graphene-based electrochemical device with thermoresponsive microneedles for diabetes monitoring and therapy,” *Nat. Nanotechnol.*, vol. 11, no. 6, pp. 566–572, 2016. DOI: 10.1038/nnano.2016.38.

[9] Y. Zhang, *et al.*, “Theoretical and experimental studies of epidermal heat flux sensors for measurements of core body temperature,” *Adv. Healthc. Mater.*, vol. 5, no. 1, pp. 2–127, 2016. DOI: 10.1002/adhm.201500110.

[10] H. Li, *et al.*, “Epidermal inorganic optoelectronics for blood oxygen measurement,” *Adv. Healthc. Mater.*, vol. 6, no. 9, pp. 1601013, 2017. DOI: 10.1002/adhm.201601013.

[11] W. Gao, *et al.*, “Fully integrated wearable sensor arrays for multiplexed in situ perspiration analysis,” *Nature*, vol. 529, no. 7587, pp. 509–514, 2016. DOI: 10.1038/nature16521.

[12] C. Lu, *et al.*, “A thermal analysis of the operation of microscale, inorganic light-emitting diodes,” *Proc. R. Soc. A*, vol. 468, no. 2146, pp. 3215–3223, 2012. DOI: 10.1098/rspa.2012.0225.

[13] M. Sakai, Y. Yamazaki, S. Yamaguchi, J. Hayashi and K. Kudo, “Mechanical analysis of organic flexible devices by finite element calculation,” *Physica Status Solidi (a)*, vol. 211, no. 4, pp. 795–799, 2014. DOI: 10.1002/pssa.201330151.

[14] D. Kang, *et al.*, “Ultrasensitive mechanical crack-based sensor inspired by the spider sensory system,” *Nature*, vol. 516, no. 7530, pp. 222–226, 2014. DOI: 10.1038/nature14002.

[15] Y. Cui, Z. Bian, Y. Li, Y. Xing and J. Song, “3D thermal analysis of rectangular microscale inorganic light-emitting diodes in a pulsed operation,” *J. Phys. D: appl. Phys.*, vol. 49, no. 40, pp. 405101, 2016. DOI: 10.1088/0022-3727/49/40/405101.

[16] L. Zhong, *et al.*, “When nanocellulose meets liquid metal: a review of the synergistic frontier for flexible electronics,” *Cellulose*, vol. 32, no. 17, pp. 9787–9818, 2025. DOI: 10.1007/s10570-025-06808-0.

[17] S. Seema and A. Singhal. Mechanics of SH and anti-plane SH waves in orthotropic piezoelectric quasicrystal with multiple surface effect. *Acta Mech.*, 236(1):439–456, 2025. DOI: 10.1007/s00707-024-04162-z.

[18] S. Seema and A. Singhal. Theoretical investigation of SH wave transmission in magneto-electro-elastic structure having imperfect interface using approximating method. *Appl. Phys. A*, 130(8):597, 2024. DOI: 10.1007/s00339-024-07744-9.

[19] A. Singhal, “Investigation of surface and interface effects of piezoelectric quasicrystal different models with propagation of shear horizontal and anti-plane shear horizontal wave,” *Acta Mech. Sin.*, vol. 41, no. 11, pp. 524389, 2025. DOI: 10.1007/s10409-024-24389-x.

[20] E. Carrera, M. Cinefra, M. Petrolo and E. Zappino, *Finite Element Analysis of Structures through Unified Formulation*. Chichester, West Sussex, UK: John Wiley & Sons, 2014.

[21] A. Entezari, M. Filippi and E. Carrera, “Unified finite element approach for generalized coupled thermoelastic analysis of 3D beam-type structures. Part 1: equations and formulation,” *J. Thermal Stresses*, vol. 40, no. 11, pp. 1386–1401, 2017. DOI: 10.1080/01495739.2017.1336740.

[22] M. Filippi, A. Entezari and E. Carrera, “Unified finite element approach for generalized coupled thermoelastic analysis of 3D beam-type structures, Part 2: numerical evaluations,” *J. Thermal Stresses*, vol. 40, no. 11, pp. 1402–1416, 2017. DOI: 10.1080/01495739.2017.1336741.

[23] M. Filippi, E. Carrera and A. M. Zenkour, “Static analyses of FGM beams by various theories and finite elements,” *Compos. Part B: Eng.*, vol. 72, pp. 1–9, 2015. DOI: 10.1016/j.compositesb.2014.12.004.

[24] E. Carrera, M. Cinefra and F. A. Fazzolari, “Some results on thermal stress of layered plates and shells by using unified formulation,” *J. Thermal Stresses*, vol. 36, no. 6, pp. 589–625, 2013. DOI: 10.1080/01495739.2013.784122.

[25] R. Azzara, M. Filippi and E. Carrera, “Coupled thermoelastic transient analyses of truss-like structures via high-fidelity beam models,” *J. Thermal Stresses*, vol. 48, no. 12, pp. 1529–1547, 2025. DOI: 10.1080/01495739.2025.2518459.

[26] R. B. Hetnarski, M. R. Eslami and G. M. L. Gladwell, *Thermal Stresses: Advanced Theory and Applications*, volume 158. New York, USA: Springer, 2009.

[27] J. N. Reddy, *An Introduction to Nonlinear Finite Element Analysis: With Applications to Heat Transfer, Fluid Mechanics, and Solid Mechanics*. New York, USA: Oxford University Press, 2015.

[28] A. Entezari, “Solution of coupled thermoelasticity problem in rotating disks,” PhD thesis, Politecnico di Torino, Turin, Italy, 2017.

[29] N. M. Newmark, “A method of computation for structural dynamics,” *J. Engrg. Mech. Div.*, vol. 85, no. 3, pp. 67–94, 1959. DOI: 10.1061/JMCEA3.0000098.

[30] R. Azzara, E. Carrera, M. Filippi and A. Pagani, “Time response stress analysis of solid and reinforced thin-walled structures by component-wise models,” *Int. J. Str. Stab. Dyn.*, vol. 20, no. 14, pp. 2043010, 2020. DOI: 10.1142/S0219455420430105.

[31] R. Azzara, M. Filippi and A. Pagani, "Variable-kinematic finite beam elements for geometrically nonlinear dynamic analyses," *Mech. Adv. Materi. Structures*, vol. 30, no. 20, pp. 4146–4154, 2023. DOI: 10.1080/15376494.2022.2091185.

[32] H. R. Meyer-Piening, "Application of the elasticity solution to linear sandwich beam, plate and shell analyses," *Jnl. Sandwich Structures Mater.*, vol. 6, no. 4, pp. 295–312, 2004. DOI: 10.1177/1099636204035395.

[33] J. Zhang, Y. Li and Y. Xing, "Theoretical and experimental investigations of transient thermo-mechanical analysis on flexible electronic devices," *Int. J. Mech. Sci.*, vol. 160, pp. 192–199, 2019. DOI: 10.1016/j.ijmecsci.2019.04.041.

[34] S. H. Nguyen, N. N. Nam, T. D. Hoang, T. N. Nguyen and T. Nguyen-Thoi, "Alpha assumed rotations and shear strains for spatially isotropic polygonal reissner-mindlin plate elements," *Comput. Structures*, vol. 274, pp. 106900, 2023. DOI: 10.1016/j.compstruc.2022.106900.

[35] S. H. Nguyen and D. H. Phan, "Selective element domain interpolation technique for assumed rotations and shear strains in polygonal finite element thick/thin plate analysis," *Thin-Walled Structures*, vol. 186, pp. 110677, 2023. DOI: 10.1016/j.tws.2023.110677.